Research Square

Preprints are preliminary reports that have not undergone peer review.
They should not be considered conclusive, used to inform clinical practice,
or referenced by the media as validated information.

Subaerial volcanic trigger of ocean productivity recovery after the Toarcian Oceanic Anoxic Event

Gong Yanjie

gyj2008vip@163.com

PetroChina Research Institute of Petroleum Exploration and Development

Caineng Zou

PetroChina Research Institute of Petroleum Exploration and Development https://orcid.org/0000-0001-5912-1729

Thomas Algeo

University of Cincinnati

Ruoyu Sun

Tianjin University https://orcid.org/0000-0001-7261-8377

Zihu Zhang

Article

Keywords: Early Jurassic, Arc volcanism, Mercury isotopes, Chemical weathering, Redox, Neuquen Basin

Posted Date: August 12th, 2026

DOI: https://doi.org/10.21203/rs.3.rs-10286401/v1

License: This work is licensed under a Creative Commons Attribution 4.0 International License.
Read Full License

Additional Declarations: There is **NO** Competing Interest.

Abstract

During the Toarcian Oceanic Anoxic Event (T-OAE, ~ 183 Ma), marine primary productivity (MPP) exhibited pronounced spatial heterogeneity, with limited organic carbon burial in many regions and unclear mechanisms for its subsequent recovery. Here, we present high resolution mercury isotopes, nitrogen and sulfur isotopes, iron speciation, and redox data from a marine sedimentary succession in the Neuquén Basin, Argentina, to investigate post T-OAE MPP recovery in a back-arc setting. Our results demonstrate that subaerial arc volcanism significantly intensified terrestrial chemical weathering (CIA from ~ 46 to ~ 70), enhancing terrestrial phosphorus input to the ocean. The resulting phosphorus supply exceeded nitrogen availability, triggering nitrogen fixation ($\delta^{15}N_{bulk}$ from + 13.81‰ to + 2.81‰), which effectively alleviated nitrogen limitation and sustained elevated MPP (TOC from < 1 wt% to 3.75 wt%). The increased organic carbon burial further promoted the upward migration of the sulfate reduction zone toward the sediment–water interface, enhancing sulfate supply and sulfur isotopic fractionation (as recorded by strongly negative $\delta^{34}S_{py}$ values). This study demonstrates that regional arc volcanism acted as a key driver of post T-OAE marine productivity recovery by modulating weathering and nutrient cycling, providing new insights into the recovery of marine ecosystems after a major oceanic anoxic event.

1. Introduction

The Toarcian Oceanic Anoxic Event (T-OAE), at ~ 183 Ma, was a major global geological event [1]. During the T-OAE, there were significant perturbations in the global carbon cycle [2], climatic warming [2], regional marine anoxia [3], and changes in biodiversity [4]. In addition, MPP increases during the T-OAE exhibited remarkable spatial heterogeneity [5, 6, 7]. Whereas increases in total organic carbon (TOC) are recorded across northwestern Europe and other areas such as the Lusitanian Basin in Portugal [8], the Betic Cordillera in Spain [9], the Southern Alps in the southern Tethys [10], the High Atlas in northern Gondwana, Morocco [11]; northern Chile in southwestern Gondwana [12], and the northern and southern parts of the Neuquén Basin (Arroyo Lapa North) of Argentina in western Gondwana [7] all show no apparent increase in TOC content.

The spatial heterogeneity of MPP and organic matter preservation has been attributed to varying paleogeographic settings and regional circulation patterns [2, 11], climate-driven nutrient supply [5, 13], enhanced storm activity during the T-OAE [6], and differences in sedimentation rates and burial rates [5, 14]. However, the post-T-OAE recovery of marine productivity in these regions remains poorly studied, and the driving factors are still unclear.

Recent detailed investigations have documented important phenomena of rapid post-T-OAE productivity recovery. The Neuquén back-arc basin in Argentina is one of the most thoroughly studied basins for the T-OAE globally [7, 12, 15, 16]. Numerous tuff layers from the Andean volcanic arc to the west of the basin provide precise age constraints [16], and the latest biostratigraphic and geochemical data offer

high-resolution records across the T-OAE, enabling inter-section correlation [7]. Among these, the Arroyo Serrucho section in the northern Neuquén Basin exhibits low TOC values during the T-OAE [7], providing a favorable setting for our study. In this contribution, we present carbon, mercury, nitrogen, sulfur isotope data, iron speciation, and major/trace element data from shales and ash layers of the Arroyo Serrucho section, allowing us to assess the role of regional volcanism in controlling MPP and organic carbon burial.

2. Materials and methods

2.1. Materials

The Neuquén Basin is located east of the Andes, between 32° and 41°S in west-central Argentina and central Chile (Fig. 1). It is a Mesozoic back-arc rift basin formed during the breakup of Gondwana and the subsequent opening of the South Atlantic [16], with Jurassic arc volcanism to the west (Fig. 1B). Samples were collected from the Arroyo Serrucho (AS) section, which is situated at Serrucho Creek in the northern part of the Neuquén Basin (Fig. 1A), received its sediments primarily from western Jurassic arc volcanism and northeastern cratonic sources [15]. The geochemical data from the Las Overas (LO) section, located 1 km away, can be well correlated with those from the AS section [7]. The studied interval comprises a 127.5-m-thick succession of the Tres Esquinas Formation. The lower part of the Tres Esquinas Formation consists of organic-rich black shales with local carbonaceous siltstones, carbonate and abundant tuff layers (Fig. 2). It was deposited on the outer continental shelf with water depths of no more than 200 m [16]. Two tuff layers at depths of 40.1 m and 48.2 m (corresponding to 18.3 m and 21.9 m in Mazzini et al., 2010) yielded high-quality ID-TIMS U–Pb zircon ages of 182.16 ± 0.6 Ma and 180.16 ± 0.66 Ma, respectively [16] These ages, together with biostratigraphic calibration covering the upper Pliensbachian to Toarcian (from the *tenuicostatum* to lower *Dumortieria* and Andean ammonite zones) and chemostratigraphic records [7], constrain the time scale of our section from the Lower Toarcian *bifrons* Zone to the Upper Toarcian *pseudoradiosa* Zone of the European Subboreal Zonation [7]. The base of our section lies 20 m above the top of the T-OAE negative carbon isotope excursion (CIE) (Fig. 1C).

All samples were collected from outcrops. Each sample was inspected and rinsed with deionized water before crushing to ensure freshness. Carbon analyses were performed at the Institute for Energy Technology (IFE) at Kjeller, Norway, and the University of Oslo. Mercury concentration and isotope analyses were carried out at Tianjin University. Iron speciation and sulfur isotopes were analyzed at Chengdu University of Technology. TOC, nitrogen content and isotopes, and major/trace elements were measured at Wuhan Sample Solution Analytical Technology Co., Ltd. Backscattered electron microscopy was performed at Zhongke Baice Testing Company to observe framboidal pyrite and measure their sizes.

2.2 Carbon analyses

The bulk sediment samples for organic carbon isotopes were ground and 50 mg of powder was treated with 5 mL portions of 2-N HCl for decarbonation. This process was repeated until no more CO_2 was released. The samples were then cleaned with portions of 5 mL distilled water until neutral pH was reached and then dried in an oven at 80°C overnight. The samples were weighed and approximately 5 mg was transferred to 9×15 mm tin capsules. The combustion of the samples was done in the presence of O_2 and Cr_2O_3 at 1700°C with a Carlo Erba NCS 2500 element analyser. Water was removed on a chemical trap of $Mg(ClO_4)_2$ before separation of N_2 and CO_2 on a 2 m Poraplot Q GC column. Carbon content (wt%) was quantified on the basis of the Thermal Ionization Detector results from the GC. The CO_2 was directly injected on-line to a Micromass Optima, Isotope Ratio Mass Spectrometer for determination of $\delta^{13}C$. To establish of a two point calibration line, USGS24 and an internal reference graphite were analysed together with the samples. Results are reported in δ notation, as per-mil (‰) deviation relative to the VPDB standard. The precision for $\delta^{13}C$ is 0.1‰ (2SD).

The total organic carbon (TOC) contents were measured on powdered samples by oxidation of organic matter to CO/CO_2 between 300 and 650°C with a LECO CR-412 at the Department of Geosciences of the University of Oslo.

2.2 Mercury proxy analyses

For Hg content analysis the DMA-80 evoHg analyzer was employed, and the testing involved four sequential steps: thermal decomposition, catalytic cracking, amalgamation, and atomic absorption detection. Samples first underwent a freeze-drying step, followed by thermal decomposition to release Hg. The decomposed products were carried by a continuous oxygen flow into a catalytic cracking tube, in which halogens (chlorine, bromine, iodine), nitrogen, and sulfur oxides were captured, and all Hg species were reduced to elemental mercury (Hg(0)). Hg(0) was then transported using an oxygen carrier gas to a gold amalgamation tube for selective trapping. Finally, the amalgamation tube was heated to release Hg into the atomic absorption spectrophotometer for detection. Analytical precision and accuracy were assessed using periodically measured certified reference materials (CRMs). Combined 1SD analytical uncertainties were < 6% for THg concentrations (DORM-4, NIST 3133). Replicate analyses ($n \geq 2$) yielded relative standard deviations (RSDs) of < 6% for THg. Procedural blanks contained < 4% of the Hg mass in the corresponding samples. One replicate sample was analyzed every ten samples.

Hg-isotope analysis: A multi-collector inductively coupled plasma mass spectrometer (MC-ICP-MS, Nu Plasma 3D) was employed for this study. The MC-ICP-MS operates by ionizing samples via a high-temperature plasma (~ 7000°C), followed by magnetic deflection of charged particles to separate and measure isotope ratios. During Hg-isotope determination, nine Faraday cups simultaneously collected Hg and Tl isotopes: ^{196}Hg, ^{198}Hg, ^{199}Hg, ^{200}Hg, ^{201}Hg, ^{202}Hg, ^{203}Tl, ^{204}Hg, and ^{205}Tl. Mass-dependent and mass-independent fractionation values of Hg-isotopes were calculated based on these ratios:

$$\delta^{x}Hg = [(^{x}Hg/^{198}Hg)_{sample}/(^{x}Hg/^{198}Hg)_{std} - 1] \times 1000 \quad (1)$$

where ^{x}Hg is ^{199}Hg, ^{200}Hg, ^{201}Hg, or ^{202}Hg, and “std” represents the NIST SRM 3133 mercury standard. The MDF is reported as δ^{202}Hg, and MIF is reported as the capital delta notation (Δ) according to the following equation:

$$\Delta^{x}Hg = \delta^{x}Hg - (\delta^{202}Hg \times \beta) \quad (2)$$

where *x* is the mass number of Hg-isotopes 199, 200, and 201. β is a scaling constant used to estimate the theoretical kinetic MDF, and it is 0.2520, 0.5024, and 0.7520 for ^{199}Hg, ^{200}Hg, and ^{201}Hg, respectively.

To correct mass discrimination effects during instrumental analysis, this study applied internal normalization with thallium (Tl) and standard-sample bracketing (SSB). The SSB method involves analyzing NIST SRM 3133 Hg standard before and after each sample, ensuring matrix and concentration matching between standards and samples. For internal normalization, Tl isotopes with masses close to Hg are simultaneously measured during Hg-isotope analysis. The mass fractionation factor (β) is calculated based on the known and measured Tl-isotope ratios, which is then used to correct the Hg-isotope ratios in samples. The Tl solution was introduced into the instrument via a membrane desolvation nebulizer along with Hg(0) vapor. Prior to sample analysis, instrumental parameters were optimized to achieve optimal peak shape and signal intensity. To monitor instrument stability and accuracy, NIST SRM 8610 standard and CRM GBW07405 are analyzed every five samples, with reported δ^{202}Hg values of − 0.55 ± 0.05‰ (1SD, *n* = 8) and − 1.72 ± 0.01‰ (1SD, *n* = 8), respectively, consistent with previous studies [17].

After each sample or standard analysis, the reaction tube is cleaned with 5% mixed acid (HNO_3: HCl = 2:1) to reduce the blank signal to < 0.2% of the previous sample/standard’s δ^{202}Hg signal, effectively eliminating memory effects and cross-contamination to ensure measurement precision.

2.3 Iron speciation and $\delta^{34}S_{py}$

For iron speciation, the method of (Li et al., 2015) was used to quantify iron in oxides (Fe_{ox}), carbonates (Fe_{carb}), magnetite (Fe_{mag}) and pyrite (Fe_{Py}). Content of Fe_{Py} was calculated stoichiometrically from pyrite sulphur (FeS_2) which was extracted by using $CrCl_2$ reduction method and precipitated as Ag_2S in silver nitrate traps. One or two pure pyrite standards (Alfa Aesar) were extracted for each batch, generating a recovery uniformly higher than 90%. Carbonate iron (Fe_{carb}), oxide iron (Fe_{ox}), magnetite iron (Fe_{mag}) were measured using a sequential extraction procedure described by [18]. About 100mg of sample powder were treated at 50°C for 48 h in a sodium acetate solution adjusted to a pH of 4.5 by addition of analytical-grade acetic acid to extract Fe_{carb}. The residual sample from the first step was treated at room temperature for 2 h in a 50 g/L sodium dithionite solution adjusted to a pH of 4.8 by addition of 0.2 M sodium citrate and analytical-grade acetic acid to extract Fe_{ox}. The residual sample from the second step was further treated at room temperature for 6 h in a 0.2-M ammonium oxalate and 0.17-M oxalic acid solution adjusted to a pH of 3.2 by addition of analytical-grade ammonia water to extract Fe_{mag}. All

extracts were diluted by 2% nitric acid, and Fe contents were determined using an atomic absorption spectroscope (AAS) with RSD of < 5%. Two international shale standards (KL133 and KL134) were used for quality control of the sequential extraction with standard deviation of measured values from the recommended values ≤ 0.1% for KL133 and ≤ 0.1% for KL134 [19].

For $\delta^{34}S_{py}$, excess V_2O_5 was mixed with the extracted Ag_2S and measured on a Thermo-Fisher Scientific Delta Q isotope-ratio mass spectrometer (IRMS) coupled with a Flash elemental analyzer (EA). The δ^{34}Spy values were reported in δ-notation relative to the international standard of Vienna Cañon Diablo Troilite (VCDT) in the form of $\delta^{34}S_{py}$ =([^{32}/^{34}Ssample]/[^{32}/$^{34}S_{VCDT}$] 1) × 1,000. Three IAEA standards, S1 ($\delta^{34}S$ = 0.3‰), S2 ($\delta^{34}S$ = + 22.7‰), and S3 ($\delta^{34}S$ = 32.3‰), two China National Standard material GBW04414 ($\delta^{34}S$ = − 0.07‰) and GBW04415 ($\delta^{34}S$ = 22.15‰) were used to monitor and calibrate pyrite or sulfide analytical results during S-isotope analysis, yielding a precision better than 0.2‰ (1σ). Three IAEA standards, NBS-127 ($\delta^{34}S$ = + 21.1‰), IAEA-SO-5 ($\delta^{34}S$ = + 0.49‰) and IAEA-SO-6 ($\delta^{34}S$ = − 34.05‰), were used to monitor and calibrate CAS, barite or sulfate mineral analytical results during S-isotope analysis, yielding a precision better than 0.2‰ (1σ).

2.4 Total nitrogen (TN) and $\delta^{15}N$ analyses

The testing was determined using an EA Isolink CN/HO elemental analyzer coupled to a DELTA Q isotope ratio mass spectrometer (IRMS, Thermo Scientific) via a Conflo IV universal continuous-flow interface, employing a rapid combustion method. Based on the nitrogen content of the samples, aliquots (≤ 20 mg) were weighed into tin capsules, compacted into spherical pellets, and introduced into the combustion reactor (980°C) of the elemental analyzer via an autosampler. The samples were combusted under a high-purity oxygen atmosphere. The resulting gaseous products were subsequently reduced, dried, and separated on a chromatographic column (60°C) to obtain purified N_2 gases. These purified gases were then introduced into the DELTA Q IRMS through the Conflo IV interface for analysis. Linear corrections were applied using international reference materials, including glutamic acid, urea, soils, and sediments. The analytical precision (standard deviation) was better than 0.3‰.

2.5 Major- and trace-element analyses

The sample pretreatment of whole rock for major element analysis was made by the melting method. The flux is a mixture of lithium tetraborate, lithium metaborate, and lithium fluoride (45:10:5). Ammonium nitrate and lithium bromide were used as oxidants and release agents, respectively. The melting temperature was 1050°C and the melting time was 15 minutes.

Zsx Primus II wavelength dispersive X-ray fluorescence spectrometer (XRF) produced by RIGAKU, Japan was used for the analysis of major elements in the whole rock. The X-ray tube is a 4.0 Kw end window Rh target, the test conditions are voltage: 50 kV, current: 60mA, and all major element analysis lines are kα, the standard curve uses the national standard material: rock standard sample GBW07101-14, soil standard sample GBW07401-08, stream sediment standard sample GBW07302-12. The data were corrected by the theoretical α coefficient method. The relative standard deviation (RSD) is less than 2%.

Trace element analysis of whole rocks was conducted on an Agilent 7700e ICP-MS at the Wuhan Sample Solution Analytical Technology Co., Ltd., Wuhan, China. The detailed sample-digesting procedure was as follows: (1) Sample powder (200 mesh) were placed in an oven at 105 ℃ for drying of 12 hours; (2) 50 mg sample powder was accurately weighed and placed in a Teflon bomb; (3) 1 mL HNO_3 and 1 mL HF were slowly added into the Teflon bomb; (4) Teflon bomb was putted in a stainless steel pressure jacket and heated to 190 ℃ in an oven for > 24 hours; (5) After cooling, the Teflon bomb was opened and placed on a hotplate at 140 ℃ and evaporated to incipient dryness, and then 1 mL HNO_3 was added and evaporated to dryness again; (6) 1 mL of HNO_3, 1 mL of MQ water and 1 mL internal standard solution of 1ppm In were added, and the Teflon bomb was resealed and placed in the oven at 190 ℃ for > 12 hours; (7) The final solution was transferred to a polyethylene bottle and diluted to 100 g by the addition of 2% HNO_3.

3. Results

3.1 Productivity proxies

TOC contents show a clear three-stage pattern (Unit 1 low, Unit 2 high, Unit 3 intermediate), with Unit 2 further subdivided into onset (TOC increasing), body (TOC high), and recovery (TOC decreasing) (Fig. 2). Unit 1 (depth ~ 155.4–162 m): TOC (0.4 ± 0.33 wt%, 1SD) and Ni_{EF} (0.33 ± 0.15) are low. Unit 2 (depth ~ 104.2–155.4 m): TOC (~ 2 wt%) and Ni_{EF} (~ 0.87) are significantly higher than Unit 1 (Fig. 2, Table 1). Onset stage (~ 144.1–155.4 m): TOC (1.81 ± 0.63 wt%) and Ni_{EF} (0.76 ± 0.19) increase markedly. Body stage (~ 130.5–144.1 m): TOC (up to 3.75 wt%) and Ni_{EF} (up to 1.37) reach maxima. Recovery stage (~ 104.2–130.5 m): TOC oscillates downward, Ni_{EF} decreases (0.81 ± 0.25). Unit 3 (~ 30.5–104.2 m): TOC (2.07 ± 0.47 wt%) and Ni_{EF} (0.61 ± 0.21) are lower than Unit 2 but still above Unit 1.

3.2 Mercury concentrations *and isotopes*

Hg concentrations are generally low(27.96 ± 20.21 ng/g, 1SD, Fig. 2), and the Hg content in tuff layers is also not high (28.02 ± 15.17 ng/g, 1SD, Fig. 2). The $\Delta^{199}Hg$ and $\Delta^{200}Hg$ values show little variation throughout the section, mostly fluctuating around 0‰. A t-test (two-sample assuming equal variances) performed on the combined Unit 1–3 dataset versus Unit 2 data yields p = 0.48 and 0.42 for $\Delta^{199}Hg$ and $\Delta^{200}Hg$, respectively, indicating that the Hg isotope data of Unit 2 are not significantly different from those of the other two units. In addition, $\delta^{202}Hg$ values range from − 2.5‰ to − 0.5‰, and also show no obvious differences among the three stages (p = 0.42).

3.3 Weathering indices and redox proxies

In Unit 1, the chemical weathering index CIA (< 50) and Al/Zr (< 0.02) are both low, C/N < 15, and $\delta^{13}C_{org}$ is relatively positive (>−25‰). $\delta^{15}N$ is relatively high at 9.75 ± 5.84‰, whereas $\delta^{34}S_{Py}$ is relatively low at − 20.74 ± 11.08‰ (Fig. 2). Iron speciation data show Fe_{HR}/Fe_T > 0.38, Fe_{Py}/Fe_{HR} < 0.8, and the redox

proxies Mo_{EF} (1.43 ± 0.56, 1SD), U_{EF} (1.18 ± 0.24, 1SD), and U/Th (0.26 ± 0.05, 1SD) are all low. C_{org}/P (mol) is low (< 20).

In the onset stage of Unit 2 (~ 144.1–155.4 m), CIA and Al/Zr increase markedly to 65.23 ± 3.53 and 0.03 ± 0.00, respectively. C/N > 20, δ^{13}Corg shows a significant negative excursion to a minimum of − 29.8‰. δ^{15}N decreases to 5.80 ± 1.38‰. $\delta^{34}S_{Py}$ rises to − 13.58 ± 4.49‰. Iron speciation shows Fe_{HR}/Fe_T ranges from 0.5 to 0.8, Fe_{Py}/Fe_{HR} increases markedly to a maximum of 0.84. Mo_{EF} (1.57 ± 0.39, 1SD), U_{EF} (4.49 ± 2.31, 1SD), and U/Th (0.30 ± 0.07, 1SD) all increase significantly. C_{org}/P (78.64 ± 16.52, 1SD) rises to nearly four times that of Unit 1, but Mo/TOC (1.59 ± 0.42, 1SD) shows little change.

In the body stage, CIA (64.4 ± 3.17, 1SD) and Al/Zr (0.03 ± 0.01, 1SD) remain high. C/N (24.17 ± 6.79, 1SD) remains high, and $\delta^{13}C_{org}$ stays negative with a minimum of − 29.7‰. δ^{15}N further decreases to a minimum of 3.84‰, while $\delta^{34}S_{py}$ shows an opposite trend to δ^{15}N, decreasing to − 16.78 ± 6.6‰ (1SD). Iron speciation is consistent with the onset stage, with Fe_{Py}/Fe_{HR} ranging from 0.5 to 0.8 and a maximum of 0.61. Redox proxies Mo_{EF} (17.12 ± 11.62, 1SD), U_{EF} (2.45 ± 1.08, 1SD), and U/Th (0.48 ± 0.21, 1SD) further increase to their maxima. C_{org}/P (80.4 ± 36.6, 1SD) remains high, and Mo/TOC (7.55 ± 4.67, 1SD) increases significantly.

In the recovery stage, CIA (66.01 ± 3.72, 1SD), Al/Zr (0.04 ± 0.00, 1SD), and C/N (23.8 ± 6.83, 1SD) continue to remain high, and $\delta^{13}C_{org}$ stays negative with a minimum of − 29.3‰. δ^{15}N further decreases to a minimum of + 2.81‰. $\delta^{34}S_{py}$ shows the same negative trend as δ^{15}N, decreasing to − 20.77 ± 6.78‰. In iron speciation, Fe_{Py}/Fe_{HR} shows little change, but Fe_{Py}/Fe_{HR} markedly decreases, with a maximum of only 0.03. Redox proxies Mo_{EF} (9.88 ± 6.16, 1SD), U_{EF} (1.91 ± 0.44, 1SD), and U/Th (0.40 ± 0.09, 1SD) begin to decline but remain relatively high. C_{org}/P (83.54 ± 34.6, 1SD) continues to remain high, and Mo/TOC (5.48 ± 3.12) begins to decrease.

In Unit 3, CIA (60.83 ± 5.03, 1SD) and Al/Zr (0.03 ± 0.00, 1SD), C/N (30.67 ± 10.02, 1SD) show some decrease compared to the recovery stage but are still higher than in Unit 1. $\delta^{13}C_{org}$ (−27.01 ± 1.43‰, 1SD), δ^{15}N (7.03 ± 1.9‰, 1SD), and $\delta^{34}S_{py}$ (−16.76 ± 8.21‰, 1SD) begin to shift positively. In iron speciation, Fe_{Py}/Fe_{HR} and Fe_{Py}/Fe_{HR} show little change compared to the recovery stage. Redox proxies Mo_{EF} (3.09 ± 1.34, 1SD), U_{EF} (1.44 ± 0.20, 1SD), and U/Th (0.31 ± 0.04, 1SD) further decrease. C_{org}/P (79.29 ± 35.98, 1SD) is higher than in Unit 1, while Mo/TOC (1.62 ± 1.35, 1SD) decreases markedly.

3.4 Framboidal pyrite

Framboidal pyrite is mainly developed in Unit 2, and is relatively less abundant in Units 1 and 3. Particle size statistics show that the overall mean diameter is 13 ± 7 μm, with average values of 17 ± 12 μm (*n* = 3, 1SD), 13 ± 6 μm (*n* = 7, 1SD), and 11 ± 7 μm (*n* = 3, 1SD) for Units 1, 2, and 3, respectively. All the above data are detailed in Table 1.

4. Discussion

4.1 Low MPP after T-OAE

After the end of the T-OAE, the organic carbon isotopes of the basin gradually returned from the significantly negative values during the T-OAE(–27.9 ± 2.86‰, cf.[15])to the background level of Unit 1 (–24.58 ± 2.33‰, Table 1). The scarcity of tuff layers indicates that the western arc volcanism had not yet intensified significantly at this time. The low CIA (< 50) and Al/Zr (< 0.02) values indicate that the weathering rate was significantly reduced compared to the T-OAE period (Al/Zr, 0.03 ± 0.01, cf. [7], and the flux of terrigenous nutrients to the ocean was low. The TOC content in this interval was generally maintained at a low level, reflecting a relatively impoverished marine primary productivity [20] that was not driven by large-scale nutrient input. Redox-sensitive elements (Mo, U, C_{org}/P) were depleted in the basin, but the iron speciation Fe_{HR}/Fe_T ratio was greater than 0.38, and framboidal pyrite was relatively undeveloped, indicating intermittent anoxic–dysoxic conditions [21] coexisting with generally insignificant sulfide burial [22]. The very low Mo/TOC values reflect a strongly restricted watermass environment (Fig. 3). Overall, this interval represents a pre-recovery stagnant stage of low productivity and relative anoxia, transitional from the extreme T-OAE environment to normal paleoceanographic conditions. The nitrogen isotope (9.75 ± 5.84‰) and sulfur isotope (–20.74 ± 11.08‰) data indicate that, in a ferruginous suboxic water column, denitrification [23] intensified the consumption of the nitrogen reservoir, while sulfate reduction likely occurred mainly in the deep sediments [22].

4.2 Intense arc volcanism and enhanced terrigenous input

Our target section contains 14 tuff layers that are related to the ancient Andean arc magmatism (Fig. 2), directly recording the intense Jurassic arc volcanic eruptions to the west of the basin [16]. The tuff layers range in thickness from a few centimeters to 5–10 cm, displaying a typical bentonite appearance consisting of white clay that turns brown after surface weathering [16]. The thickness of these tuff layers generally indicates volcanic eruptions with a Volcanic Explosivity Index of 6 or above, with eruption volumes of tens to hundreds of cubic kilometers [24].

Although volcanic ash is abundant, the mercury concentrations in the samples are not high, which may be attributed to post-depositional preservation conditions. Mercury released by volcanic eruptions tends to escape in gaseous form, and during ash settling or diagenesis, if subjected to high-temperature degassing, hydrothermal alteration, or prolonged weathering and leaching, the adsorbed mercury can be oxidized and released [25]. In addition, volcanic ash with low organic matter content lacks effective carriers for mercury sequestration, making mercury enrichment difficult [26]. Therefore, the low mercury values in ash-rich horizons more likely reflect post-depositional loss rather than a primary input deficiency. In this section, mercury shows a good correlation with nickel (R^2 = 0.49;n = 13;p < 0.01) but poor correlations with other host-phase elements, suggesting that nickel-bearing sulfide-related

components are likely the main host phase for mercury (Fig. S1). A detailed description of the mercury host phases is provided in Supplemental Note1.

The MIF characteristics of mercury show near-zero values, with Δ^{199}Hg mainly ranging from − 0.05‰ to + 0.02‰ and a mean value of − 0.01 ± 0.02‰, and Δ^{200}Hg mainly ranging from − 0.04‰ to + 0.03‰ with a mean value of − 0.01 ± 0.02‰ (Fig. 2, Table 1). This is most likely caused by mixing of mercury inputs from terrestrial sources and mercury deposition from arc volcanic emissions. The main sources of terrestrial mercury are the uptake of atmospheric Hg(0) by vegetation (subsequently input through litterfall) and the direct uptake of Hg(0) by soils, and terrestrial plants and soils that uptake Hg(0) typically exhibit negative Δ^{199}Hg and Δ^{200}Hg values. Previous studies have reported that mercury deposition associated with arc volcanic emissions generally has positive Δ^{199}Hg values [27], which is attributed to the recycling of oceanic mercury into the mantle lithosphere via subduction of oceanic slabs [27], while marine mercury generally has positive Δ^{199}Hg and Δ^{200}Hg values. Therefore, mixing of multiple mercury sources may produce intermediate Δ^{199}Hg values (i.e., near zero), particularly in coastal environments [28]. We cannot exclude the possibility of mercury input from bedrock weathering, because weathering not only introduces mercury from terrestrial soils and sedimentary rocks but also mercury derived from bedrock weathering (Δ^{199}Hg ≈ 0‰, similar to mantle sources, cf. [27]). However, as noted above, the main sources of terrestrial mercury are the uptake of atmospheric Hg(0) by vegetation and soils, and the proportion of mercury from bedrock may be relatively small.

Nevertheless, the Δ^{199}Hg values of LIP basalts are also generally near zero, because the lower mantle lacks recycled mercury [27]. Direct LIP emissions from the mantle, if without long-range transport and thus without experiencing photochemical redox reactions that generate isotope fractionation [25], are generally considered to have negative δ^{202}Hg and near-zero Δ^{199}Hg and Δ^{200}Hg values [29]. However, major-element, trace-element, and rare-earth element geochemical analyses of tuffs from the Neuquén Basin [30] all indicate that these ash layers originated from the western arc volcanism [31, 32]. Moreover, even the relatively nearby Karoo volcanic province is approximately 1000 km away from the Neuquén Basin [31], so it is unlikely that the mercury signal from LIP emissions could have remained as mantle-derived signals without experiencing photochemical redox reactions and isotopic fractionation during long-range transport.

Volcanic activity is generally considered to be an important factor in inducing intensified continental weathering [33, 34, 35]. Volcanic eruptions release large amounts of CO_2, enhancing the greenhouse effect and causing a significant rise in surface temperature. Elevated temperatures accelerate the chemical decomposition of silicate and other minerals, while also enhancing hydrological cycling and runoff scouring capacity, thus significantly increasing the weathering rates of continental rocks. This mechanism has been widely documented throughout Earth's history [33, 35]. Weathering indices, including the Chemical Index of Alteration (CIA) and the corrected CIA (CIA*), the CaO-free Chemical Index of Alteration (CIX) and the corrected CIX (CIX*), were generally used to quantify the intensity of subaerial chemical weathering [35, 36], and the formulas and detailed calculation descriptions are provided in

Supplemental Note2. The Al/Zr ratio has a similar indicative significance to CIA, as aluminum is relatively stable and enriched during chemical weathering, while zirconium (mainly hosted in resistant zircon) accumulates in the weathering residue as a highly stable element [37]. Our Al/Zr and CIA data show that, compared to Unit 1 (CIA: 48.87 ± 4.82, 1SD; Al/Zr: 0.02 ± 0.00, 1SD, Table 1), Unit 2 has higher CIA (65.16 ± 3.29, 1SD, Table 1) and Al/Zr (0.04 ± 0.01, 1SD, Table 1), indicating an increase in terrigenous chemical weathering intensity. The watermass restriction indicator Mo/TOC [38] shows a significant increase in Unit 2, indicating reduced water restriction (Fig. 4A). The salinity proxy B/Ga has a mean value of 2.77 (± 0.56). It should be noted that, due to the acid digestion method used for trace element analysis, the loss rate of B is approximately 32% [39], so the actual B/Ga value is likely ~ 3.97, which probably reflects brackish overall salinity conditions resulting from terrestrial freshwater input (Fig. 4B).

4.3 Enhanced nutrient flux and MPP

TOC can serve as an effective proxy for MPP [20]. Since there is no evidence for significant changes in sedimentation rate within the 127.5-m section of the Tres Esquinas Formation in the northern Neuquén Basin [7, 16], the duration of organic carbon enrichment (Unit 2, depth ~ 104.2–155.4 m, TOC > 2%) can be estimated as approximately 1.3 Myr based on the zircon U–Pb dating data of two tuff layers at depths of 40.1 m and 48.2 m. In Unit 2 after the end of the T-OAE, the peak TOC values are accompanied by a significant negative excursion in $\delta^{13}C_{org}$ (from − 23.4‰ to − 29.8‰, Fig. 2 and Table 1), which may be related to the enhanced input of terrigenous C3 plants (with average $\delta^{13}C$ values of approximately − 27‰ to − 28‰, cf. [40]) due to intensified weathering. The input lead to a marked increase in sedimentary TOC content and a negative excursion in $\delta^{13}C_{org}$ toward the characteristic values of C3 plants [41]. The elevated TOC together with C/N > 10 (Fig. 2) also indicates a significant input of terrigenous higher plants [42]. The dense occurrence of tuff layers in Unit 2, together with the fact that TOC contents in black shales reached up to nearly 4 wt%, implies a close link between volcanically driven nutrient input and MPP. The frequent input of volcanic ash not only brought large amounts of volcaniclastic material to the basin, but also significantly enhanced the transport of terrigenous (including volcanic-derived) nutrients to the ocean [36, 43]. Therefore, the intense arc volcanism and its associated terrigenous material input exerted a major influence on the carbon cycle and productivity state after the T-OAE.

The increase in terrigenous chemical weathering intensity, as indicated by elevated CIA or Al/Zr, promotes the input of terrigenous nutrients to the ocean, thereby enhancing primary productivity. The close link between enhanced chemical weathering and its driven nutrient input and primary productivity increase is clearly supported by sedimentary records from various geological intervals, including the early Paleozoic [44], mid-Proterozoic[36], Mesozoic oceanic anoxic events [45], Paleocene-Eocene Thermal Maximum [46]. Our observational data from the AS section, together with previously published data from the LO section [7], also show the same pattern. TOC exhibits significant positive correlations with Al/Zr (R^2 = 0.56, n = 28, p < 0.01, Fig. 5A) and CIA (R^2 = 0.47, n = 28, p < 0.01, Fig. 5B). For the LO section, CIA data were not published previously; we therefore estimated them using the strong positive correlation

between CIA and Al/Zr established from the AS section (R^2 = 0.75, n = 31, p < 0.01). In marked contrast to the post-T-OAE interval, the T-OAE in the LO section shows almost no correlation between TOC and weathering indices (R^2 < 0.01, n = 54, p > 0.01, Fig. 5A and B). The nickel (Ni) content in sediments is generally strongly linearly correlated with organic matter flux and has better preservation than carbon, making it a reliable proxy for settling organic matter flux [47]; while the increase in the carbon/phosphorus burial ratio (C_{org}/P) can serve as an indicator for tracking terrigenous organic carbon input and reflecting changes in terrestrial net primary productivity [48]. Our data show that Ni_{EF} (R^2 = 0.22, n = 28, p < 0.01, the AS and LO sections) and C_{org}/P (R^2 = 0.61, n = 28, p < 0.01; The published data for the LO section do not include phosphorus) exhibit significant positive correlations with CIA (Fig. 5C and 5D), i.e., they increase significantly with increasing weathering intensity, which also indirectly supports the regulation of MPP by weathering intensity.

Volcanic phosphorus sources are considered to be an important mechanism for ocean fertilization throughout Earth's history [49]. In addition, when chemical weathering is intensified, phosphorus and other elements in rocks can also be effectively released, and enhanced weathering and erosion promote the transport of dissolved phosphorus and other nutrients to the ocean [45]. Phosphorus, as a key limiting nutrient in the long-term regulation of marine primary productivity, can directly promote MPP and carbon fixation rates with increased input from volcanism or enhanced weathering [50]. However, if a strongly euxinic environment exists at the sediment–water interface, excess phosphorus supply may not be reflected as elevated phosphorus content in the sediments [51], because such redox conditions promote phosphorus recycling [52], which is manifested as elevated organic carbon/phosphorus (C_{org}/P) ratios without increased phosphorus content [48]. This is consistent with our observations. Compared to Unit 1, Unit 2 shows no increase in phosphorus content (Fig. 2), but the C_{org}/P ratio increases significantly (from 11.9 ± 8.46 in Unit 1 to 80.4 ± 36.6 in the Unit 2 body stage, Fig. 2 and Table 1).

Nitrogen isotope and sulfur isotope data also support the increase in MPP. From Unit 1 to the onset stage of Unit 2, sulfur isotopes show a positive shift (from − 20.74 ± 11.08‰ to − 13.58 ± 4.49‰), while nitrogen isotopes show a negative shift (from 9.75 ± 5.84‰ to 5.80 ± 1.38‰, Fig. 2 and Table 1). Changes in $\delta^{15}N_{bulk}$ are generally related to water-column conditions [53, 54], and likely indicate that nitrogen limitation led to enhanced nitrogen fixation [54, 55]. Arc volcanic eruptions, combined with enhanced continental weathering together drove a surge in marine phosphorus input. When phosphorus supply exceeds nitrogen, the relative enrichment of phosphorus becomes a driver of nitrogen limitation, which in turn strongly stimulates the metabolic activity of nitrogen-fixing microorganisms to compensate for nitrogen deficiency in the ecosystem [56]. The moderately restricted watermass environment (as indicated by the significantly increased Mo/TOC values in Unit 2, Fig. 3 and Table 1) is also conducive to nitrogen fixation [57]. This enhanced nitrogen fixation effectively alleviated nitrogen limitation [58], thereby increasing biological pump efficiency and carbon fixation rates [59], promoting the recovery of MPP, and significantly enhancing organic carbon burial fluxes [60].

Unlike nitrogen isotopes, the variation of $\delta^{34}S_{py}$ in sedimentary columns is significantly modulated by depositional environmental conditions [61]. In ferruginous environments, framboidal pyrite is more likely to form in sediments/pore waters [62]. Our framboidal pyrite particle size statistics (12.3 ± 9.1 μm, Fig. 2) also confirm that sediment, rather than the water column, was the main environment of formation [62]. When the organic carbon flux to the ocean increases, microbial sulfate reduction (MSR) activity in sediments is enhanced [63], leading to rapid sulfate consumption and directly resulting in a decrease in the overall $\delta^{34}S_{Py}$ values in the sedimentary record (i.e., reduced fractionation). This is reflected in the significant negative correlation between sulfur and nitrogen isotopes from Unit 1 to the onset stage of Unit 2 (R^2 = 0.83; p < 0.01; n = 9, Fig. 5E). Therefore, these variations in nitrogen and sulfur isotopes most likely were both driven by MPP.

The Fe_{HR}/Fe_T ratio greater than 0.38 (Fig. 3 and Table 1) indicates that sedimentation occurred in anoxic waters from Unit 1 to Unit 3 [21], suggesting that marine anoxia could persist for a considerable period after the end of the T-OAE. The same phenomenon has also been observed in the post-T-OAE sedimentary intervals of the Western Canada Sedimentary Basin and the South German Basin [64]. From Unit 1 to Unit 3, Fe_{Py}/Fe_{HR} is mostly less than 0.8, indicating ferruginous (anoxic, Fe(II)-bearing) water conditions [65] which is likely the result of volcanic aerosol emissions further amplifying the feedback of MSR. However, in the onset and body stages of Unit 2, FePy/FeHR approaches 0.8, indicating enhanced euxinic conditions [65]. In anoxic environments, pyrite sulfur isotope values in euxinic settings are generally lower than those in ferruginous settings, because sulfate concentrations in euxinic waters are typically higher than in ferruginous waters at similar depths [66]. However, our data show the opposite pattern, i.e., the sulfur isotopes in the euxinic Unit 2 body stage are higher than those in the ferruginous recovery stage, suggesting that other factors may have been involved. In the Unit 2 body stage, the significant increases in Mo_{EF} (from 1.43 ± 0.56 in Unit 1 to 17.12 ± 11.62) and U_{EF} (from 1.18 ± 0.24 in Unit 1 to 2.45 ± 1.08) indicate further intensification of anoxia [67]. When oxygen penetration depth is shallow, the initiation position of MSR is closer to the sediment–water interface [68]. As a result, the diffusion distance of seawater sulfate to the MSR zone in the sediments is shorter, the sulfate buffering capacity in pore waters is stronger, and sulfate concentration changes slowly, leading to a higher degree of isotope fractionation and the formation of lower pyrite $\delta^{34}S_{Py}$ values [69]. In other words, this process further promotes the upward shift of sulfate reduction depth from deeper sediments to positions closer to the sediment–water interface, thereby enhancing sulfate supply efficiency and isotopic fractionation. This is reflected in the gradual positive shift of $\delta^{34}S_{Py}$ toward Unit 3 (from − 20.77 ± 6.78‰ in the Unit 2 recovery stage to − 16.76 ± 8.21‰ in Unit 3), showing a positive correlation with the positive shift in nitrogen isotopes (from 4.32 ± 1.39‰ in the Unit 2 recovery stage to 7.03 ± 1.9‰ in Unit 3, reflecting weakening of nitrogen fixation) (R^2 = 0.25; p < 0.05; n = 16, Fig. 5F).

Unit 3 is characterized by TOC (2.07 ± 0.47%) and Ni_{EF} (0.61 ± 0.21) that are lower than in Unit 2 but still higher than in Unit 1, indicating that within this post-volcanic interval, marine productivity declined from the Unit 2 peak but remained at a relatively high level. The positive shift of $\delta^{15}N$ back to + 7.03‰

indicates weakening of nitrogen fixation and strengthening of nitrate utilization [54, 55]. CIA (60.83 ± 5.03) and Al/Zr show some decreases, suggesting a relative weakening of chemical weathering. $\delta^{13}C_{org}$ shows a slight positive shift (–27.01 ± 1.43‰) and C/N oscillates downward but remains at a relatively high value (30.67 ± 10.02), confirming that terrigenous organic matter input remained high but gradually decreased with oscillations. Unit 3 records a nutrient-overload-driven productivity "high-stand plateau," still above the initial level of Unit 1, reflecting the recovery of MPP. The redox environment is shown to be ferruginous suboxic ($Fe_{HR}/Fe_T > 0.38$, $Fe_{Py}/Fe_{HR} < 0.8$, with Mo_{EF} and U_{EF} significantly decreased to 3.09 ± 1.34 and 1.44 ± 0.20, respectively), which most likely resulted from the transition to more oxidizing conditions driven by nutrient surplus and the correspondingly elevated MPP, as net burial of organic carbon led to a rise in atmospheric oxygen [36].

5. Conclusions

Through high-resolution geochemical and isotopic analyses of the Arroyo Serrucho section in the Neuquén Basin, Argentina, this study reveals the staged recovery process of marine primary productivity after the T-OAE and its driving mechanisms. In this region, after the end of the T-OAE, arc volcanism to the west gradually intensified and enhanced continental weathering, promoting the transport of terrigenous nutrients to the ocean. Based on TOC, nitrogen and sulfur isotopes, and redox proxies, the recovery process can be divided into three units (Fig. 6). Unit 1 represents a starvation stage, characterized by weak chemical weathering and terrigenous input, dominance of denitrification, sulfate reduction occurring in deep sediments, and overall low marine productivity. Unit 2 represents a rapid recovery stage, characterized by the dense occurrence of tuff layers, enhanced chemical weathering and terrigenous input, reduced watermass restriction, phosphorus supply exceeding nitrogen supply, which drove enhanced nitrogen fixation to alleviate nitrogen limitation, accompanied by the upward migration of sulfate reduction to near the sediment–water interface, increased isotopic fractionation, enhanced euxinic conditions, and maximum organic carbon burial flux. Unit 3 represents a high-stand plateau stage, characterized by weakened volcanism and chemical weathering, with TOC and Ni_{EF} lower than in Unit 2 but still higher than in Unit 1, reduced nitrogen fixation, enhanced nitrate utilization, and productivity maintained at a relatively high level. Our findings demonstrate that regional arc volcanism and its induced weathering enhancement were the key driving factors for the rapid recovery of marine productivity after the T-OAE, and that through the modulation of nutrient cycling, they significantly influenced organic carbon burial and the recovery of marine ecosystems.

Declarations

Competing interests:

The authors declare that they have no competing interests.

Funding Statement

YJG would like to thank the Science and Technology Project (25KTKFSC275) of CNPC Research Institute of Science and Technology Co., Ltd. for support.

Author Contributions

YJG and CNZ conceived of and supervised the research. YJG wrote the original draft. YJG, RYS and ZHZ conducted data analyses. YJG, CNZ, TJA and RYS revised the manuscript, and all authors contributed to the manuscript until its final version.

Acknowledgments

We thank Adriano Mazzini for the sample and carbon analysis support; Hugh C. Jenkyns and Aisha H. Al-Suwaidi for carbon isotope data support and stratigraphic discussion; Genming Luo, Huyue Song for isotope discussion to our work. We are grateful to reviewers and editors for constructive comments that helped to improve the manuscript.

Data availability

Dataset is available at https://zenodo.org/records/20781730.

References

1. Jenkyns HC. The early Toarcian (Jurassic) anoxic event; stratigraphic, sedimentary and geochemical evidence. *American Journal of Science* 288, 101–151 (1988).
2. Ruebsam W, Reolid M, Marok A, Schwark L. Drivers of benthic extinction during the early Toarcian (Early Jurassic) at the northern Gondwana paleomargin: Implications for paleoceanographic conditions. *Earth-Science Reviews* 203, (2020).
3. Suan G, *et al.* Polar record of Early Jurassic massive carbon injection. *Earth and Planetary Science Letters* 312, 102–113 (2011).
4. Danise S, Slater SM, Vajda V, Twitchett RJ. Land-sea ecological connectivity during a Jurassic warming event. *Earth and Planetary Science Letters* 578, (2022).
5. Kemp DB, Suan G, Fantasia A, Jin S, Chen W. Global organic carbon burial during the Toarcian oceanic anoxic event: Patterns and controls. *Earth-Science Reviews*, (2022).
6. Ge Y, Han Z, Algeo TJ, Kemp DB, Wu L. Heterogeneous marine response during the Toarcian Oceanic Anoxic Event (TOAE): The potential role of storminess. *Global and Planetary Change*, (2024).

7. Storm M, *et al.* Integrated stratigraphy of Pliensbachian and Toarcian strata from the northern Neuquén Basin, Argentina. *Newsletters on Stratigraphy* 57, (2024).
8. Hesselbo SP, Jenkyns HC, Duarte LV, Oliveira LCV. Carbon-isotope record of the Early Jurassic (Toarcian) Oceanic Anoxic Event from fossil wood and marine carbonate (Lusitanian Basin, Portugal). *Earth and Planetary Science Letters*, (2007).
9. Silva RL, Ruhl M, Barry C, Reolid M, Ruebsam W. Pacing of late Pliensbachian and early Toarcian carbon cycle perturbations and environmental change in the westernmost Tethys (La Cerradura Section, Subbetic zone of the Betic Cordillera, Spain). *Geological Society London Special Publications*, (2021).
10. Ruvalcaba Baroni I, *et al.* Ocean Circulation in the Toarcian (Early Jurassic): A Key Control on Deoxygenation and Carbon Burial on the European Shelf. *Paleoceanography and Paleoclimatology*, (2018).
11. Bodin S, *et al.* Toarcian carbon isotope shifts and nutrient changes from the Northern margin of Gondwana (High Atlas, Morocco, Jurassic): Palaeoenvironmental implications. *Palaeogeography, Palaeoclimatology, Palaeoecology*, (2010).
12. Fantasia A, Föllmi KB, Adatte T, Bernárdez E, Spangenberg JE, Mattioli E. The Toarcian oceanic anoxic event in southwestern gondwana: an example from the Andean Basin, northern Chile. *Journal of the Geological Society*, (2018).
13. Fantasia A, Föllmi KB, Adatte T, Spangenberg JE, Montero-Serrano J-C. The Early Toarcian oceanic anoxic event: Paleoenvironmental and paleoclimatic change across the Alpine Tethys (Switzerland). *Global and Planetary Change*, (2018).
14. Ruebsam W, Mattioli E, Schwark L. Weakening of the biological pump induced by a biocalcification crisis during the early Toarcian Oceanic Anoxic Event. *Global and Planetary Change*, (2022).
15. Al-Suwaidi AH, *et al.* The Toarcian Oceanic Anoxic Event (Early Jurassic) in the Neuquén Basin, Argentina: A Reassessment of Age and Carbon Isotope Stratigraphy. *The Journal of Geology*, (2016).
16. Mazzini A, Svensen H, Leanza HA, Corfu F, Planke S. Early Jurassic shale chemostratigraphy and U–Pb ages from the Neuquén Basin (Argentina): Implications for the Toarcian Oceanic Anoxic Event. *Earth and Planetary Science Letters*, (2010).
17. Zou C, *et al.* Late Triassic hyperwarming and its link to nitrogen-cycle climate feedbacks. *Geochimica et Cosmochimica Acta*, (2026).
18. Poulton SW, Canfield DE. Development of a sequential extraction procedure for iron: implications for iron partitioning in continentally derived particulates. *Chemical Geology*, (2005).
19. Alcott LJ, *et al.* Development of Iron Speciation Reference Materials for Palaeoredox Analysis. *Geostandards and Geoanalytical Research*, (2020).
20. Canfield DE. Factors influencing organic carbon preservation in marine sediments. *Chemical Geology*, (1994).
21. Poulton SW, Canfield DE. Ferruginous Conditions: A Dominant Feature of the Ocean through Earth's History. *Elements*, (2011).

22. Wilkin RT, Arthur MA. Variations in pyrite texture, sulfur isotope composition, and iron systematics in the Black Sea: evidence for Late Pleistocene to Holocene excursions of the o2-h2s redox transition. *Geochimica et Cosmochimica Acta*, (2001).
23. Jenkyns HC. Geochemistry of oceanic anoxic events. *Geochemistry, Geophysics, Geosystems* 11, (2010).
24. Newhall CG, Self S. The volcanic explosivity index (VEI) an estimate of explosive magnitude for historical volcanism. *Journal of Geophysical Research*, (1982).
25. Grasby SE, Them TR, Chen Z, Yin R, Ardakani OH. Mercury as a proxy for volcanic emissions in the geologic record. *Earth-Science Reviews* 196, (2019).
26. Frieling J, *et al.* Effects of redox variability and early diagenesis on marine sedimentary Hg records. *Geochimica Et Cosmochimica Acta* 351, 78–95 (2023).
27. Yin R, *et al.* Mantle Hg isotopic heterogeneity and evidence of oceanic Hg recycling into the mantle. *Nature Communications*, (2022).
28. Shen J, Yin R, Algeo TJ, Svensen HH, Schoepfer SD. Mercury evidence for combustion of organic-rich sediments during the end-Triassic crisis. *Nature Communications*, (2022).
29. Sherman LS, Blum JD, Nordstrom DK, McCleskey RB, Barkay T, Vetriani C. Mercury isotopic composition of hydrothermal systems in the Yellowstone Plateau volcanic field and Guaymas Basin sea-floor rift. *Earth and Planetary Science Letters*, (2009).
30. Spalletti LA, Queralt I, Matheos SD, Colombo F, Maggi J. Sedimentary petrology and geochemistry of siliciclastic rocks from the upper Jurassic Tordillo Formation (Neuquén Basin, western Argentina): Implications for provenance and tectonic setting. *Journal of South American Earth Sciences*, (2008).
31. Al-Suwaidi AH, *et al.* New age constraints on the Lower Jurassic Pliensbachian–Toarcian Boundary at Chacay Melehue (Neuquén Basin, Argentina). *Scientific Reports*, (2022).
32. Schiuma M, Llambías E. New ages and chemical analysis on Lower Jurassic volcanism close to the dorsal de Huincul, Neuquén. *Revista de la Asociacion Geologica Argentina* 63, 644–652 (2008).
33. Gernon TM, *et al.* Global chemical weathering dominated by continental arcs since the mid-Palaeozoic. *Nature Geoscience*, (2021).
34. Shen J, *et al.* Intensified continental chemical weathering and carbon-cycle perturbations linked to volcanism during the Triassic–Jurassic transition. *Nature Communications*, (2022).
35. Zhang P, *et al.* Four volcanically driven climatic perturbations led to enhanced continental weathering during the Late Triassic Carnian Pluvial Episode. *Earth and Planetary Science Letters*, (2023).
36. Zhang S, *et al.* Subaerial volcanism broke mid-Proterozoic environmental stasis. *Science Advances*, (2024).
37. Canfield DE, *et al.* Long-term history of continental weathering and particle transport to the sea. *Proceedings of the National Academy of Sciences of the United States of America*, (2025).

38. Algeo TJ, Lyons TW. Mo-total organic carbon covariation in modern anoxic marine environments: Implications for analysis of paleoredox and paleohydrographic conditions. *Paleoceanography and Paleoclimatology*, (2006).
39. Wei W, *et al.* Evaluation of sample pretreatment methods for boron concentration analysis. *Chemical Geology*, (2025).
40. Kohn MJ. Carbon isotope compositions of terrestrial C3 plants as indicators of (paleo)ecology and (paleo)climate. *Proceedings of the National Academy of Sciences of the United States of America*, (2010).
41. Ishiwatari R, *et al.* A 35kyr record of organic matter composition and δ13C of n-alkanes in bog sediments close to Lake Baikal: Implications for paleoenvironmental studies. *Organic Geochemistry*, (2009).
42. Zhang J, *et al.* Source identification of sedimentary organic carbon in coastal wetlands of the western Bohai Sea. *Science of the Total Environment*, (2023).
43. Liu Q, *et al.* Volcanic fertilization of Late Triassic lacustrine algal blooms. *Communications Earth & Environment*, (2025).
44. Wei G-Y, *et al.* Lithium isotopic constraints on the evolution of continental clay mineral factory and marine oxygenation in the earliest Paleozoic Era. *Science Advances*, (2024).
45. Gernon TM, *et al.* Solid Earth forcing of Mesozoic oceanic anoxic events. *Nature Geoscience*, (2024).
46. Pogge von Strandmann PAE, *et al.* Lithium isotope evidence for enhanced weathering and erosion during the Paleocene-Eocene Thermal Maximum. *Science Advances*, (2021).
47. Bruggmann S, McManus J, Archer C, Vance D, Severmann S. Nickel's behaviour in marine sediments under aerobic to anaerobic diagenetic conditions. *Chemical Geology*, (2024).
48. Algeo TJ, Ingall E. Sedimentary Corg:P ratios, paleocean ventilation, and Phanerozoic atmospheric pO2. *Palaeogeography, Palaeoclimatology, Palaeoecology*, (2007).
49. Wu Y, *et al.* Enhanced erosion by continental arc volcanism as a driver of the Cambrian Explosion. *Nature Communications*, (2025).
50. Yamamoto A, Hajima T, Yamazaki D, Noguchi Aita M, Ito A, Kawamiya M. Competing and accelerating effects of anthropogenic nutrient inputs on climate-driven changes in ocean carbon and oxygen cycles. *Science Advances*, (2022).
51. Dijkstra N, *et al.* Phosphorus dynamics in and below the redoxcline in the Black Sea and implications for phosphorus burial. *Geochimica et Cosmochimica Acta*, (2018).
52. Papadomanolaki NM, Lenstra WK, Wolthers M, Slomp CP. Enhanced phosphorus recycling during past oceanic anoxia amplified by low rates of apatite authigenesis. *Science Advances*, (2022).
53. Algeo T, Rowe H, Hower JC, Schwark L, Herrmann A, Heckel P. Changes in ocean denitrification duringLate Carboniferous glacial–interglacialcycles. *Nature Geoscience*, (2008).
54. Algeo TJ, Meyers PA, Robinson RS, Rowe H, Jiang GQ. Icehouse–greenhouse variations in marine denitrification. *Biogeosciences*, (2014).

55. Luo G, *et al.* Enhanced nitrogen fixation in the immediate aftermath of the latest Permian marine mass extinction. *Geology*, (2011).
56. Jung J, *et al.* Equatorial upwelling of phosphorus drives Atlantic N2 fixation and Sargassum blooms. *Nature Geoscience*, (2025).
57. Sun X, Fan D, Hu L, Wang H. Global patterns and drivers of nitrogen isotope signal in modern marine sediments. *Nature Communications*, (2025).
58. Du Y, *et al.* Recovery from persistent nutrient-N limitation following the Permian–Triassic mass extinction. *Earth and Planetary Science Letters*, (2022).
59. Chang C, Algeo TJ. Nitrogen cycling and marine redox evolution during the Ediacaran–Cambrian transition. *Global and Planetary Change*, (2024).
60. Stüeken EE, Pellerin A, Thomazo C, Johnson BW, Duncanson S, Schoepfer SD. Marine biogeochemical nitrogen cycling through Earth's history. *Nature Reviews Earth & Environment*, (2024).
61. Mertens C, Paradis S, Hemingway JD. Sedimentary conditions drive modern pyrite burial flux to exceed oxidation. *Nature Geoscience*, (2025).
62. Rickard D. Sedimentary pyrite framboid size-frequency distributions: A meta-analysis. *Palaeogeography, Palaeoclimatology, Palaeoecology*, (2019).
63. Kemp ALW, Thode HG. The mechanism of the bacterial reduction of sulphate and of sulphite from isotope fractionation studies. *Geochimica et Cosmochimica Acta*, (1968).
64. Them TR, *et al.* Thallium isotopes reveal protracted anoxia during the Toarcian (Early Jurassic) associated with volcanism, carbon burial, and mass extinction [Earth, Atmospheric, and Planetary Sciences]. *Proceedings of the National Academy of Sciences of the United States of America*, (2018).
65. Poulton SW, Krom MD, Raiswell R. A revised scheme for the reactivity of iron (oxyhydr)oxide minerals towards dissolved sulfide. *Geochimica et Cosmochimica Acta*, (2004).
66. Gomes ML, Hurtgen MT. Sulfur isotope systematics of a euxinic, low-sulfate lake: Evaluating the importance of the reservoir effect in modern and ancient oceans. *Geology*, (2013).
67. Algeo TJ, Tribovillard N. Environmental analysis of paleoceanographic systems based on molybdenum–uranium covariation. *Chemical Geology*, (2009).
68. Fakhraee M, Li J, Katsev S. Significant role of organic sulfur in supporting sedimentary sulfate reduction in low-sulfate environments. *Geochimica et Cosmochimica Acta*, (2017).
69. Halevy I, *et al.* Sedimentary parameters control the sulfur isotope composition of marine pyrite. *Science*, (2023).

Table

Table 1 is available in the Supplementary Files section.

Figures

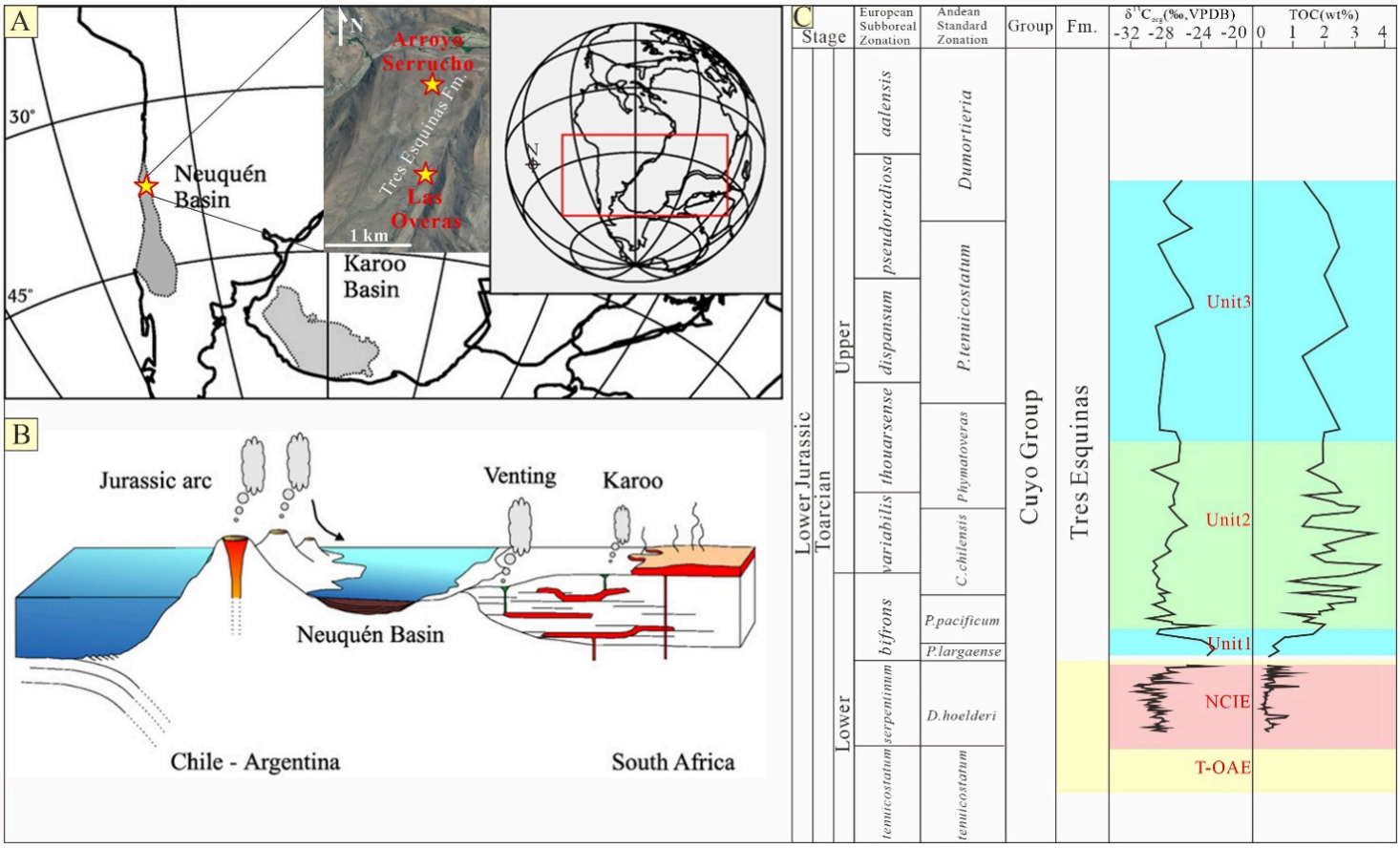


Figure 1

Location and geological context of the study area. (A) Palaeogeography of the Neuquén basin and the AS section and the LO section (shown in pentagram) at 180 Ma (Toarcian). (B) Cartoon (not to scale) of the geological setting during the Early Toarcian (A and B modified after [16] and [7]. During the initial spreading of Pangea, South Africa and Chile–Argentina were separated by the Neuquén Basin in which anoxic sediments were deposited. The tuff layers were derived from Jurassic arc volcanism in the west. (C) Epoch, standard NW European biozones, Andean ammonite zonation, group and formations of the study interval (highlighted in light green) are modified after [7]. The carbon isotope and TOC data of the NCIE interval are from [15]

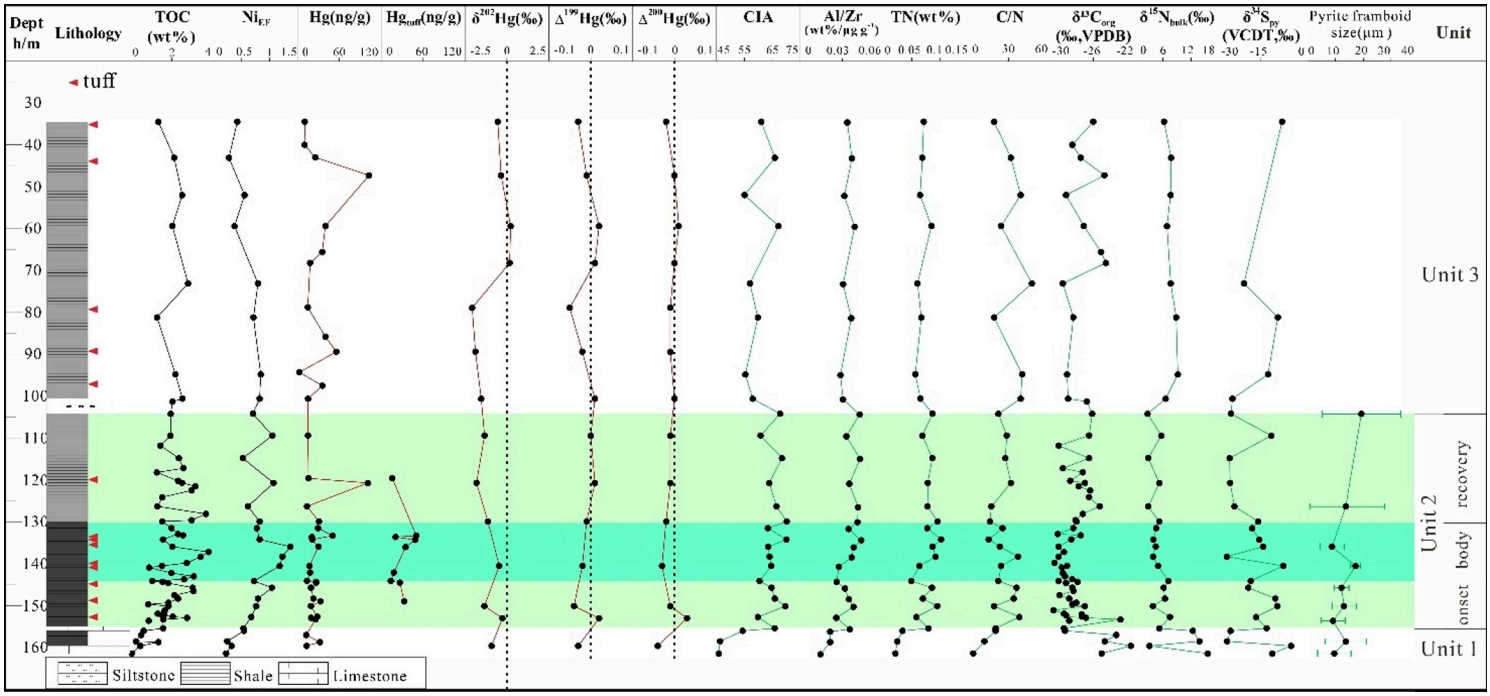


Figure 2

Chemostratigraphic profiles of the Arroyo Serrucho section in the Neuquén Basin. The black dashed line in the mercury profile represents the zero value. The error bars for the mean diameter of framboidal pyrite represent two standard deviations (2SD), where sample size $n > 30$. We converted height in Mazzini et al. (2010) to depth, so that the position of the 10–25 m CIE in that study corresponds to the 130–155 m interval in our study.

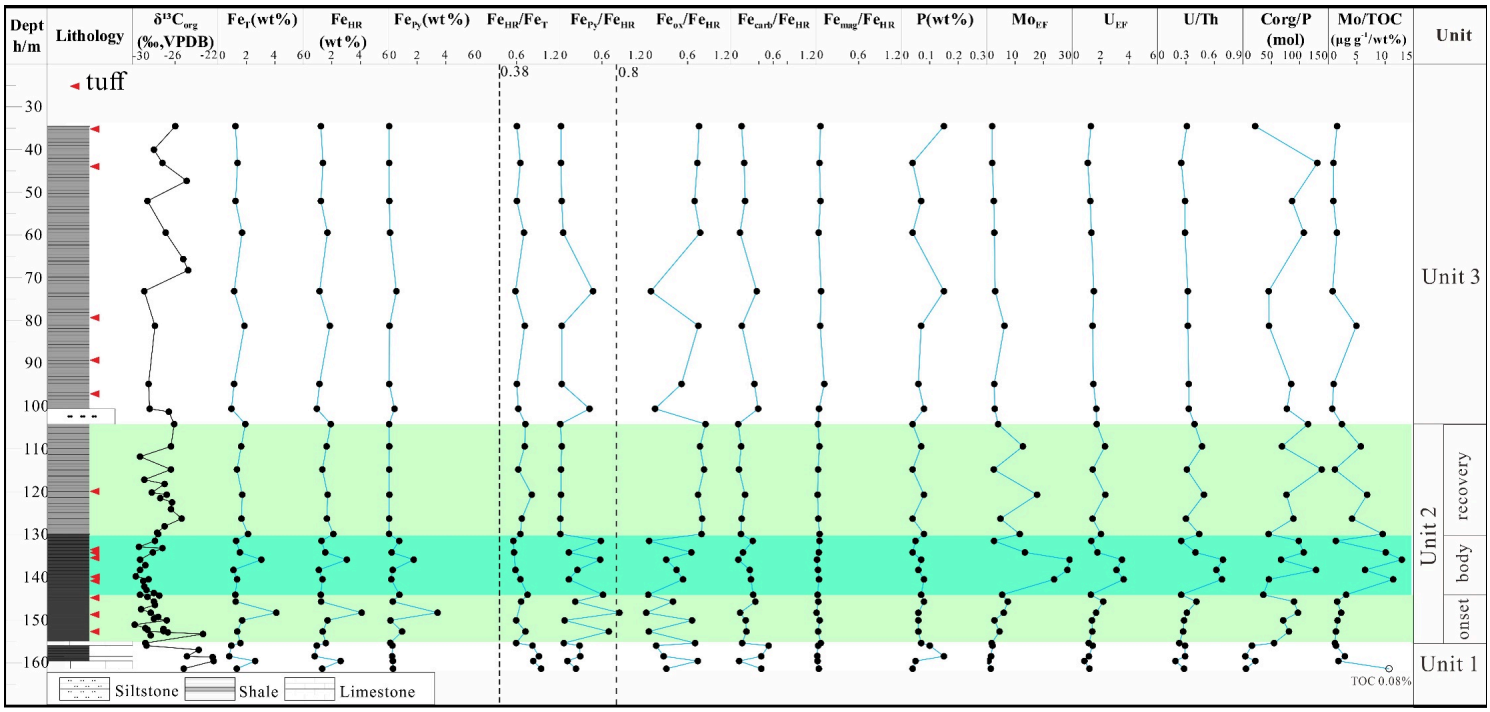


Figure 3

Redox proxy profiles of the Arroyo Serrucho section in the Neuquén Basin.

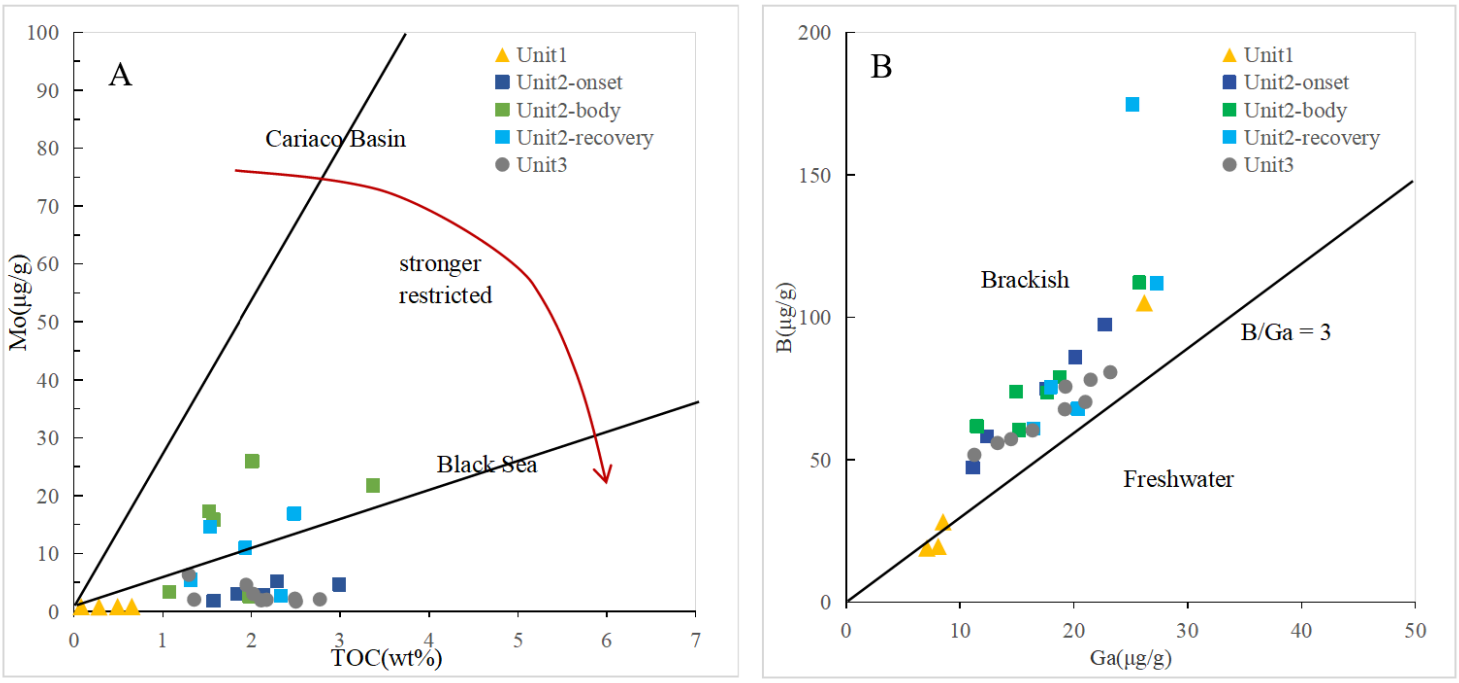


Figure 4

Crossplots of Mo vs TOC (A) and B vs Ga (B) data from the AS Section. The boron data presented here have been corrected based on the recovery rate [39].

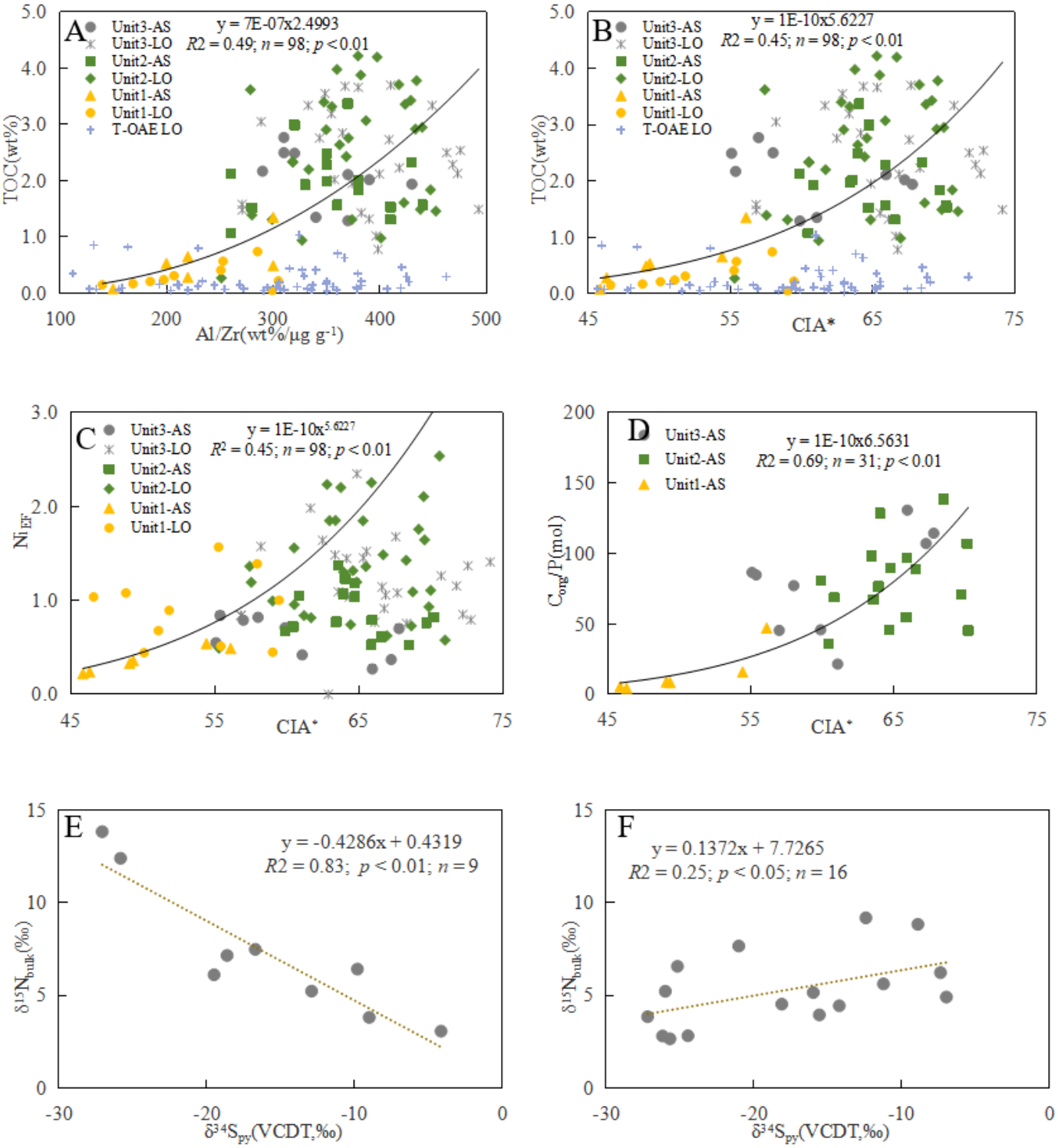


Figure 5

Crossplots of C, Hg, N elemental or isotopic data from the AS and LO sections. (A) TOC vs. CIA; (B) TOC vs. Al/Zr; (C) Ni_{EF} vs. CIA; (D) C_{org}/P vs. CIA; (E) $\delta^{15}N_{bulk}$ vs. $\delta^{34}S_{Py}$ for Unit1 and onset interval of Unit2; (F) $\delta^{15}N_{bulk}$ vs. $\delta^{34}S_{Py}$ for recovery interval of Units 2 and 3.

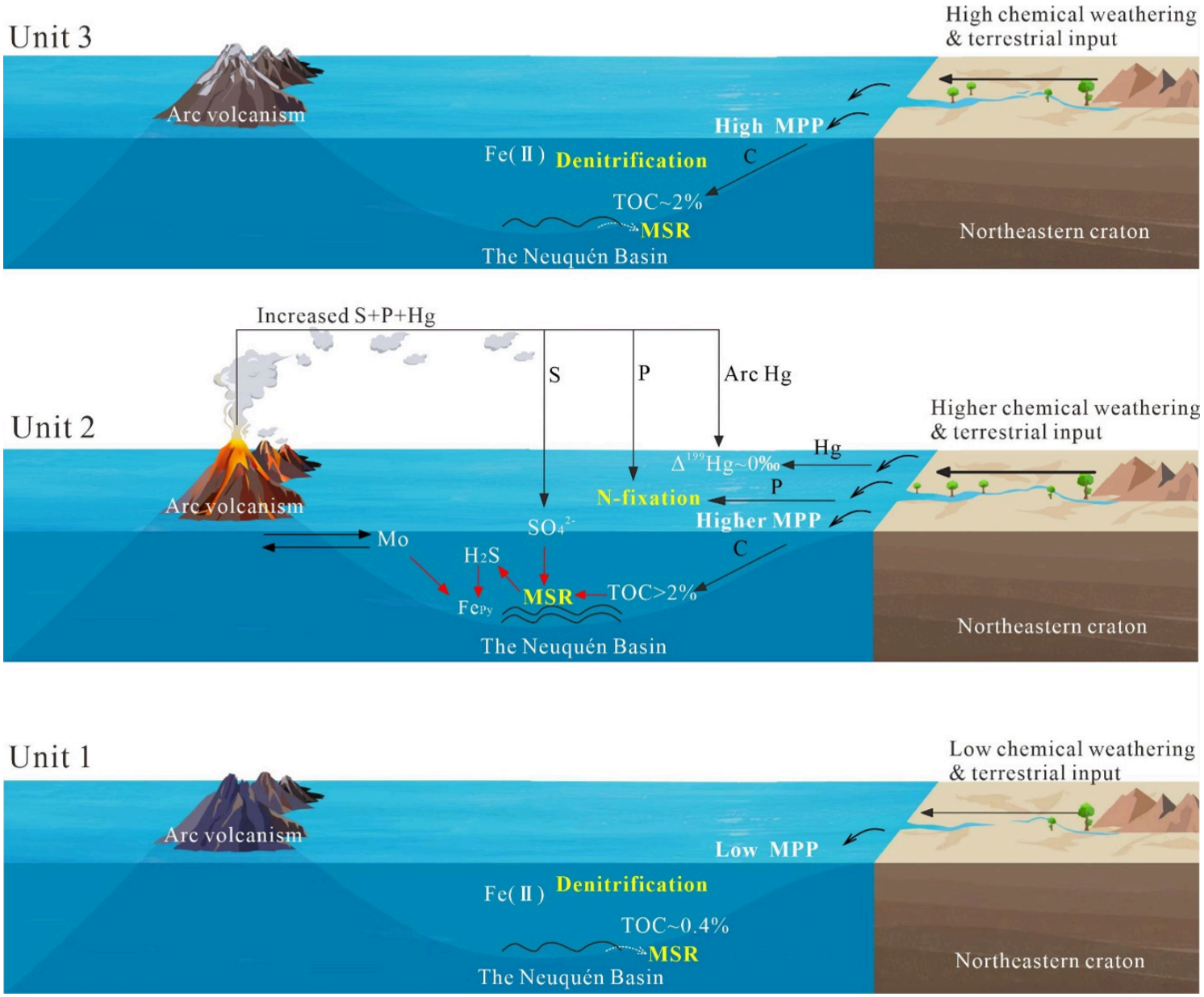


Figure 6

Impacts of arc volcanism on MPP of the Neuquén Basin after the T-OAE. The black wavy lines represent sediments; black arrows indicate material flux transport; red arrows indicate reactions or control effects. Abbreviations: MSR, Microbial Sulfate Reduction; Fe(Ⅱ), ferrous iron; S, sulfide aerosol; P, phosphorus; Hg, mercury; N, nitrogen; Mo, molybdenum.

Supplementary Files

This is a list of supplementary files associated with this preprint. Click to download.

- Dataset1.xls
- Supplementary1.docx

- Table1.docx